

Design and construction of a solar tracking system for small-scale linear Fresnel reflector with three movements

A. Barbón^a, J.A. Fernández-Rubiera^a, L. Martínez-Valledor^c, A. Pérez-Fernández^c, L. Bayón^{b,*}

^a Department of Electrical Engineering, University of Oviedo, Spain

^b Department of Mathematics, University of Oviedo, Spain

^c Polytechnic School of Engineering of Gijón, University of Oviedo, Spain

ARTICLE INFO

Keywords:

Small-scale linear Fresnel reflector
Solar tracking system
Raspberry pi

ABSTRACT

A new open-loop solar tracking system for a small-scale linear Fresnel reflector with three movements has been designed, fabricated, and simulated. The control system of the solar tracker is governed by a Raspberry Pi together with other auxiliary devices which include a Global Positioning System. The electronic control system consists of a master controller (Raspberry pi 3), 4 slave microcontrollers (Arduino), Global Positioning System module, thermocouples, laser sensors, transversal positioning sensors, and longitudinal positioning sensors. It also allows the communication between these microcontrollers based on long range wireless solutions (XBee). All the electronic circuits have been designed and constructed. The solar tracking system uses offline data. The software has been designed and developed to track the sun path using astronomical equations. In this way, the solar tracking system is able to position itself automatically using the solar position algorithm and the Global Positioning System with an accuracy of $\pm 0.006^\circ$. The solar tracking system can be deployed automatically at any location on the Earth. The total cost of the implemented solar tracking system has been calculated. The system performance, in terms of the tracking error, annual energy, energy-to-area ratio and levelized cost of energy has been evaluated. Tracking errors smaller than 0.06° are acceptable (they cause power losses smaller than 1%), whereas errors larger than 0.36° start being noticeable (power losses greater than 3%). The proposed new tracking system gives 16.64% more energy, a 78.46% higher energy-to-area ratio, and a 4.62% less levelized cost of energy that the classic tracking system with one movement used in large-scale linear Fresnel reflectors.

1. Introduction

The solar energy is one of the most important renewable energies because of its abundance (the Sun is the main source of Earth's energy) and its sustainability. As an important candidate for solar thermal utilization, the Linear Fresnel Reflector (LFR) employs a large field of rows of mirrors which are used to concentrate the sunlight on the focal line of an absorber tube with a much smaller area. The absorber tube that runs longitudinally above the mirror rows is located at the common focal line of the mirrors. The absorber tube is specially coated to increase its capability to absorb the incident sunlight and it is encased in a cavity receiver to reduce the convective heat losses. The concentrated solar energy is transferred through the absorber tube to some thermal fluid capable of maintaining itself in liquid state at high temperatures.

Linear Fresnel Reflector (LFR) technology can be used in various applications. Large-scale linear Fresnel reflectors are used in electricity generation [1,2] and in industrial processes [3,4], whereas small-scale linear Fresnel reflectors (SSLFRs) are used in the building sector [5,6].

Considering a linear Fresnel reflector aligned in a North–South orientation, the angle of incidence of solar irradiance on the absorber tube will be calculated in two projection planes [7]: the transversal incidence angle and the longitudinal incidence angle.

In the transversal plane, the secondary reflector redirects Sun beams towards the absorber tube. Different secondary reflector shapes have been proposed throughout the last years: compound parabolic design [8], involute design [9], parabolic design [9], butterfly design [10, 11], trapezoidal design [12], triangular design [13] and other complex geometries. In the longitudinal plane, not all the Sun's rays reflected

* Corresponding author.

E-mail address: bayon@uniovi.es (L. Bayón).

by the mirrors fall on the absorber tube. There is a part of the absorber tube which is not illuminated by Sun's rays, called the inactive part of the tube. This fact produces losses known as end loss [14]. On the other hand, there are Sun's rays reflected by the mirrors that do not fall on the absorber tube. These rays are known as reflected light loss [14]. The end loss efficiency can be calculated with the following equation [15]:

$$\eta_{\text{end-loss}} = \frac{L_a - L_{\text{end-loss}}}{L_a} \cdot 100 \quad (1)$$

where L_a is the length of the absorber tube and $L_{\text{end-loss}}$ is the part of the absorber tube that is not illuminated. The end losses of the absorber tube depend on: the latitude of the site, the moment when it is evaluated and the geometry of the mirrors' field [16].

In large-scale linear Fresnel reflectors, the rows of mirrors and the absorber tube form an angle of 0 (°) with the horizontal plane. In addition, due to their size, both the rows of mirrors and the absorber tube are not provided with a longitudinal movement. In this case, the rows of mirrors can be rotated on the North–South axis, so as to follow the Sun's daily movement (transversal movement). In this reflector, due to the size of the absorber tube and the height of the receiver, the end loss efficiency is approximately 97%, in Almeria (Spain) [14], and the reflected light loss is not usually considered in the mathematical expression normally used to determine the power absorbed by the absorber tube [17,15,18].

In *SSLFRs* due to the small size of the rows of mirrors and the absorber tube, in several references it is reviewed the possibility of moving these parts. Authors such as [19,20,14,21,22] describe various types of simultaneous movements. Dai et al. [19] propose a design North–South oriented with three movements: the transversal movement, the East–West translation of the entire reflector field according to the relative position of the Sun and the rotation of a secondary reflector located in the receiver. The movements proposed by [20,14] with a North–South oriented design, are: the transversal movement, the East–West axis rotation of the mirrors row and the East–West axis rotation of the absorber tube. Other prototypes present an East–West oriented design: [21] and [22]. In [21], it is presented a design that includes a reflective surface that forms a parabola and a receiver which can move along the axial axis. In [22], it is proposed a design rotated around the horizontal North–South axis, which has the possibility to adjust the tilt of the entire collector with the solar height.

In *SSLFR* without longitudinal movement, the longitudinal position and the length of the absorber tube are two critical parameters for its design [14]. The use of non-optimal values leads to decreases of up to 80% in the energy production [14]. The most favorable values of the longitudinal position and of the length of the absorber tube depend on the latitude of the site. As the economic aspect is very important to the trade of the *SSLFR*, the *SSLFR* manufacturing process could be improved if its design was independent of the latitude of the site. This goal would be achieved, providing longitudinal movement to the rows of mirrors and to the absorber tube.

The $\eta_{\text{end-loss}}$ in *SSLFR* increases as the height of the receiver decreases [14]. The most common height value of the receiver in an *SSLFR* is 1.5 (m) [23,22]. In *SSLFR* configuration with the rows of mirrors and the absorber tube parallel to the horizontal plane, the end loss efficiency is approximately 70%, for a height of the receiver of 1.5 (m) in Almeria (Spain) [14]. The design of *SSLFRs* with longitudinal movement of the rows of mirrors and the absorber tube would minimize the end loss and the reflected light loss [24].

In building sector the available area is a critical parameter. Therefore, the energy-to-area ratio (*EAR*) parameter has to be considered. The *EAR* represents the relationship between total annual energy absorbed by the absorber tube and the area required for the *SSLFR* installation. In [24] it is shown that in the *SSLFR* configurations with longitudinal movements the area required for *SSLFR* installation is significantly reduced.

There are several possible configurations of longitudinal movements. The movement of rows of mirrors may occur continuously throughout the day or just at one single time in a day. In the first group of configurations, the design ensures that for any time of the day the rays reflected by the mirrors in the longitudinal direction are always vertical to the absorber tube. In the second group of configurations, the longitudinal inclination is equal to the latitude of the place, corrected by means of the declination. In addition, the secondary reflector may have the same longitudinal movement as the rows of mirrors. In other configurations, the secondary reflector system forms a certain angle with the horizontal plane and it is not provided with longitudinal movement. The proposed new solar tracking can implement all of these configurations.

Once the advantages of an *SSLFR* with longitudinal movement of the rows of mirrors and the absorber tube have been discussed, we are going to present in this paper the design and the construction of a solar tracking system for a small-scale linear Fresnel reflector with three movements: one transversal movement, and two longitudinal movements.

The heat losses of the secondary reflector system of an *SSLFR*, depend on its longitudinal movement. Even though the heat losses increase with the increase in the longitudinal angle [25], it has been demonstrated that the longitudinal inclination of the secondary reflector system has positive effects on the efficiency of an *SSLFR* [25]. The application of a phase change material in the glazing structure can improve its thermal performance by enhancing its capacity of storing thermal energy [26,27]. On the other hand, the introduction of a corrugated insert into the absorber tube can effectively enhance the heat transfer performance [28].

The use of another technologies can also enhance the performance of an *SSLFR*. In the paper [29] the advantages of the use of nanotechnology in renewable energies are shown. In relation to solar energy, Hussein [30] shows the application of nanotechnology in various solar collectors. The performance of a direct absorption solar collector can be improved by using nanofluid technology [31]. Another example is the use of a multiwalled carbon nanotube and water nanofluid in a flat plate solar collector for the energy optimization [32].

Broadly speaking, the solar tracking strategies can generally be: open-loop control (*OLC*) [33,34], closed-loop control (*CLC*) [33,34], and hybrid control [35]. In an *OLC*, the Sun tracking system is based on a pre-programmed code according to the calculated Sun's position from formulas or algorithms using its geographic coordinates (latitude, altitude), solar time and day of the year, without using feedback signals. In a *CLC*, the Sun tracking system uses optical sensors to detect the Sun's real-time position using feedback signals. In an hybrid control mode, the solar tracking system can automatically switch between open-loop or closed-loop solar tracking strategy depending on the local weather conditions.

The *OLC* is characterized by the following advantages and disadvantages: (i) it has high reliability, (ii) it has a low tracking accuracy, it does not detect any disturbances generated in either computing or mechanical processes [36], (iii) it does not need sensors to detect sunlight, (iv) it is simple, (v) it has a low cost approach compared to the *CLC* [37], (vi) the system may not compensate its external disturbances (misalignment during setup and operation) in the system [38], (vii) it has a low capability to correct errors.

The *CLC* is characterized by the following advantages and disadvantages: (i) it is affected by the local weather conditions, therefore it has a low reliability, (ii) it is very accurate [34,39,40], (iii) it is complex.

To the best of our knowledge, there is not any design similar to this one we propose among all the previous writings about this issue. The solar tracking system can be used in a small-scale linear Fresnel reflector with one single movement. The solar tracking system has been designed and constructed. The simulated results are presented to evaluate the contrast between its performance in terms of power

absorbed by the absorber tube with and without tracking error. The proposed solar tracking system is a low cost tracker. The solar tracking system uses offline data and it is able to position itself automatically based on a Sun path algorithm and the *GPS* data, with an accuracy of $\pm 0.006^\circ$. A cloudy sky has no impact on the system operation.

The system performance has been evaluated in terms of the tracking error, annual energy, energy-to-area ratio and levelized cost of energy. Moreover, we shall see that the proposed new tracking system gives more energy (16.64%), a higher energy-to-area ratio (78.46%) and a 4.62% less levelized cost of energy than the classic tracking system with one movement used in large-scale *LFRs*.

The paper is organized as follows. The components, parameters, and relationships of an *SSLFR* are described in Section 2. The design and implementation of the proposed solar tracking system is presented in Section 3. Solar tracking system algorithms are described in Section 4. Section 5 presents the results of the study of the tracking error, energy, energy-to-area ratio, and levelized cost of energy. Finally, Section 6 summarizes its main contributions and conclusions.

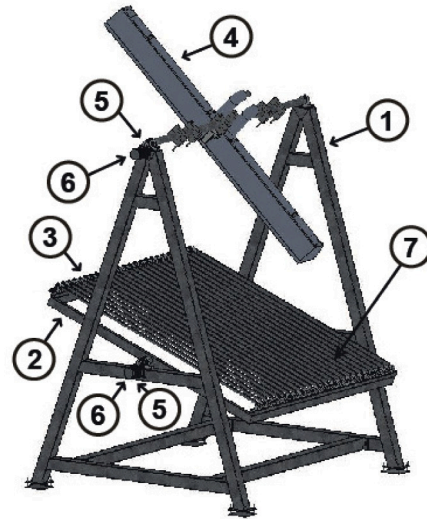


Fig. 1. SSLFR parts.



Fig. 2. Prototype.

Nomenclature

D	Diameter of the absorber tube (m)
d	Separation between two consecutive mirrors (m)
f	Height of the receiver (m)
L_a	Length of the single absorber tube (m)
L_i	Position of i th mirror ($0 \leq i \leq n$) (m)
L_i^l	L_i of the left side (m)
L_i^r	L_i of the right side (m)
L_M	Length of the mirrors (m)
n	Number of mirrors at each side of the central mirror
n_d	Day number
W_M	Width of the mirrors (m)
α_i	Angle between the vertical at the focal point and the line connecting the center point of each mirror to the focal point ($^\circ$)
α_S	Height angle of the Sun ($^\circ$)
β_a	Angle between the absorber tube and the horizontal plane ($^\circ$)
β_i	Tilt of i th mirror ($^\circ$)
β_0	Tilt of central mirror ($^\circ$)
β_i^l	β_i of the left side ($^\circ$)
β_i^r	β_i of the right side ($^\circ$)
β_M	Angle between the mirror axis and the horizontal plane ($^\circ$)
δ	Declination of the Sun ($^\circ$)
γ_S	Azimuth of the Sun ($^\circ$)
θ_l	Longitudinal incidence angle ($^\circ$)
θ_t	Transversal incidence angle ($^\circ$)
θ_z	Zenith angle of the Sun ($^\circ$)
λ	Latitude angle ($^\circ$)
Γ	Daily angle (rad)
ω	Hour angle ($^\circ$)
ω_S	Angle of sunset ($^\circ$)
$-\omega_S$	Angle of sunrise ($^\circ$)

2. Considerations on the movements of an SSLFR

2.1. SSLFR components

The experimental prototype [41] used in this study consists of six main blocks: fixed structure (*FS*) (1), mobile structure (*MS*) (2), primary reflector system (*PRS*) (3), secondary reflector system (*SRS*) (4), transmission systems (*TR*) (5), and tracking systems (*TS*) (6). Fig. 1 shows these components, and Fig. 2 shows a photograph of the prototype.

The fixed structure lies on a foundation made for this purpose. The mobile structure and the secondary reflector system are supported by

the fixed structure. The primary reflector system has been mounted on the mobile structure. The primary reflector system is made of parallel rows of stretched mirrors (7) mounted on specially designed frames. The secondary reflector system is composed of: absorber tube, receiver cavity, insulation, and glass covering. The secondary reflector system is located at an appropriate height above the primary reflector system.

This prototype we consider, makes use of a three axis tracking system. The mobile structure can be rotated on the east–west axis. The mirrors of the primary reflector system can be rotated on the north–south axis so as to follow the Sun's daily movement. Finally, the secondary reflector system can also be rotated on the east–west axis.

2.2. Sun path

As the Earth has two orbits, the Sun path is characterized by two angles. These angles are named the solar altitude angle (α_S) and the azimuth angle (γ_S) [42].

The angular solar position vs. solar time (T_S) can be calculated using a solar apparent motion trajectory model [42] as it is shown in formula (2)–(6) (Γ is the daily angle in (rad); δ is the declination of the Sun in

(°); n_d is the day number starting from the 1st of January; ω is the hour angle in (°); λ is the geographical latitude of the site in (°); α_S is the solar altitude angle in (°); γ_S is the solar azimuth angle in (°);

$$\Gamma = (n_d - 1) \frac{2\pi}{365} \quad (2)$$

$$\delta = (0.006918 - 0.399912 \cos \Gamma + 0.070257 \sin \Gamma - 0.006758 \cos 2\Gamma + 0.000907 \sin 2\Gamma - 0.002697 \cos 3\Gamma + 0.001480 \sin 3\Gamma) \cdot \frac{180^\circ}{\pi} \quad (3)$$

$$\omega = 15 \cdot (T_S - 12) \cdot \frac{180^\circ}{\pi} \quad (4)$$

$$\alpha_S = \arcsin[\sin \delta \sin \lambda + \cos \delta \cos \lambda \cos \omega] \quad (5)$$

$$\gamma_S = \text{sign}(\omega) \cdot \arccos \left[\frac{\sin \alpha_S \sin \lambda - \sin \delta}{\cos \alpha_S \cos \lambda} \right] \quad (6)$$

The zenith angle of the Sun (θ_z) is also commonly used. It is the complementary angle to the solar altitude angle of the Sun ($\theta_z = 90^\circ - \alpha_S$). When the altitude $\alpha_S = 0$, the Sun is said to rise (sunrise) or to set (sunset). From Eq. (5):

$$\cos(\omega) = -\frac{\sin \delta \sin \lambda}{\cos \delta \cos \lambda} = -\tan \delta \tan \lambda \quad (7)$$

and hence the angle of sunrise ($-\omega_s$) and of sunset (ω_s) can be calculated with:

$$\omega_s = \arccos[-\tan \delta \tan \lambda] \quad (8)$$

2.3. Transversal and longitudinal incidence angles

In order to obtain the transversal incidence angle (θ_t) and the longitudinal incidence angle (θ_l), the angle of incidence of solar irradiance is separated into two projection planes [17]. The transversal incidence angle (θ_t) is defined as the angle between the vertical and the projection of the Sun vector on the East–West plane (the plane orthogonal to the absorber tube) and the longitudinal incidence angle (θ_l) is defined as the angle between the vertical and the projection of the Sun vector on the North–South plane. These definitions are valid when the *SSLFR* is horizontally aligned and the absorber tube is aligned in the North–South orientation.

The transversal incidence angle and the longitudinal incidence angle have been determined according to equations [14]:

$$\theta_t = \arctan \left(\frac{\sin \gamma_S}{\tan \alpha_S} \right) \quad (9)$$

$$\theta_l = \arctan \left(\frac{\cos \gamma_S}{\tan \alpha_S} \right) \quad (10)$$

These angles are required to calculate the movements of the *SSLFR*.

2.4. *SSLFR* movements

Only the direct irradiation is concentrated in an *SSLFR* so it is very important to have an adequate solar tracking system. This tracking system can be classified under three categories [20]: one-axis (only transversal movement, this is the case of the movement of the mirrors), two-axis (a transversal movement and a longitudinal movement, in this case both mobile structure and secondary reflector system move) and three-axis (a transversal movement and two longitudinal movements).

2.4.1. Movement of the mirrors

As shown in [20], the movement of each mirror can be characterized by the tilt (β_i). The β_i depends on the mirror width (W_M), the distance between two mirrors (d), the number of mirrors on each side of the central mirror (n), the receiver height (f), the diameter of the absorber tube (D), and the transversal incidence angle (θ_t). Fig. 3 shows the simplified schematic front view of a generic *SSLFR*.

The tilt of each mirror has been adjusted so that the incident ray (which arrives at an angle θ_t) reaches the focal point after a single reflection. The focal plane is located at a distance f from the reflecting

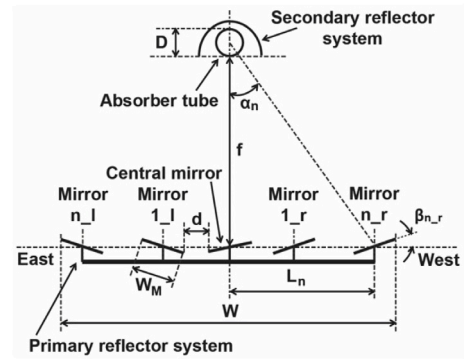


Fig. 3. Movement of the mirrors.

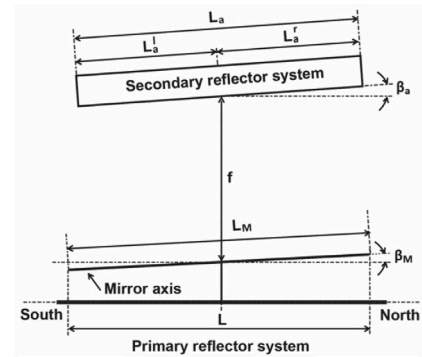


Fig. 4. Movement of the MS and SRS.

element placed in the center of the *SSLFR*. The pivot point of each mirror coincides with the central point of the mirror; therefore, it is always focused on the central point of the receiver.

In order to calculate β_i , we distinguish between: the central mirror ($i = 0$), the mirrors to the left ($1 \leq i \leq n$) and those to the right ($1 \leq i \leq n$). The total number of mirrors of the *SSLFR* is $2n + 1$. The tilt, β_i^r , on the right side is given by:

$$\beta_i^r = \frac{-\theta_t + \alpha_i}{2}; 1 \leq i \leq n \quad (11)$$

and the tilt, β_i^l , on the left side is given by:

$$\beta_i = \frac{-\theta_t - \alpha_i}{2}; 1 \leq i \leq n \quad (12)$$

Just for convenience, we consider $\beta_i^l, \beta_i^r > 0$ if they are measured counter-clockwise above the horizontal axis. For central mirror, given by:

$$\beta_0 = \frac{\theta_t}{2} \quad (13)$$

The angle α_i can be calculated as:

$$\alpha_i = \arctan \left[\frac{L_i}{f + D/2} \right]; 1 \leq i \leq n \quad (14)$$

Assuming that the *SSLFR* performs symmetrically throughout the day, the spacing between the reflecting elements on the right side is the same as that on the left side of the *SSLFR*:

$$L_i^r = L_i^l = L_i = i \cdot (W_M + d); 1 \leq i \leq n \quad (15)$$

The movement of the central mirror is the only one you have to control, the rest of the mirrors have a different starting position from the central mirror, but they all move with the same angular speed.

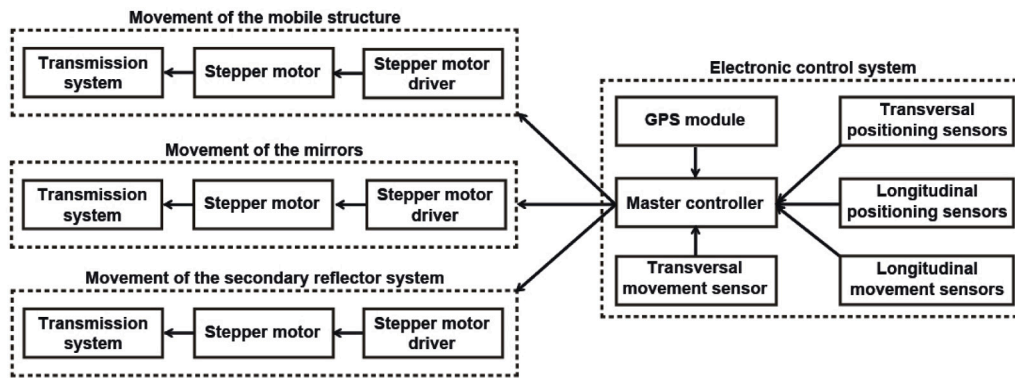


Fig. 5. Solar tracker design block diagram.

2.4.2. Movement of the mobile structure and the secondary reflector system

As shown in [20], the movement of the mobile structure and the movement of the secondary reflector system can be respectively characterized by the tilt (β_M) and the tilt (β_a). The β_M is the angle between the mirror axis and the horizontal plane. The β_a is the angle between the absorber tube and the horizontal plane. Fig. 4 shows the simplified schematic side view of a generic SSLRF.

An SSLRF can have multiple configurations [14]. The configuration in which it is fulfilled:

$$\beta_M = \beta_a = \frac{\theta_z}{2} \quad (16)$$

offers the best results [14].

This study is based on this configuration, although the other configurations can also be easily implemented.

3. Elements of the solar tracking control

The proposed solar tracking system shown in Fig. 5 consists of transmission systems, stepper motors and drivers and an electronic control system. The transmission systems of the mobile structure and the secondary reflector system are similar. The transmission system of the mirrors is different. This transmission system consists of a certain number of movement units. These movement units are defined below. The electrical hardware consists of three stepper motor and drivers. The electronic control system consists of master controller (Raspberry pi 3), slave microcontrollers (Arduino), GPS module, thermocouples, laser sensors, transversal positioning sensors, and longitudinal positioning sensors.

3.1. Mirrors movement transmission system

In Fig. 6, the mirrors (1) of the primary reflector system can be rotated on the north–south axis, so as to follow the Sun's daily movement. For this purpose, we used a rack (2) and a pinion mechanism (3). The movement requires $2 \cdot n + 1$ movement units (where n is the number of mirrors at each side of the central mirror), and a rack gear.

Each movement unit has been designed with SolidWork [43] and made as shown in Fig. 7. It includes: two bearings, two bearing supports, two shafts, a pinion gear, a mirror, a frame and a main shaft [44]. The selected elements are as follows. A standard bearing type FAG6301ZZ. A standard pinion gear with 24 teeth, module 2 (mm) and 35 (mm) thick.

A bearing support that consists of a 82.5 (mm) diameter stainless steel tube with a 20 (mm) thick wall, and a $78 \times 28 \times 5$ (mm) stainless steel plate. A shaft consists of a 25 (mm) diameter carbon steel rod 150 (mm) long. The mirror's thickness is 5 (mm). The mirror is pasted onto the frame using an industrial adhesive. The frame is a 0.8 (mm) thick galvanized steel sheet. The main shaft is a $3/8\epsilon$ diameter galvanized steel rod that is assembled to the support by stainless steel rivets. A standard rack gear with module 2 (mm) and 20 (mm) thick.

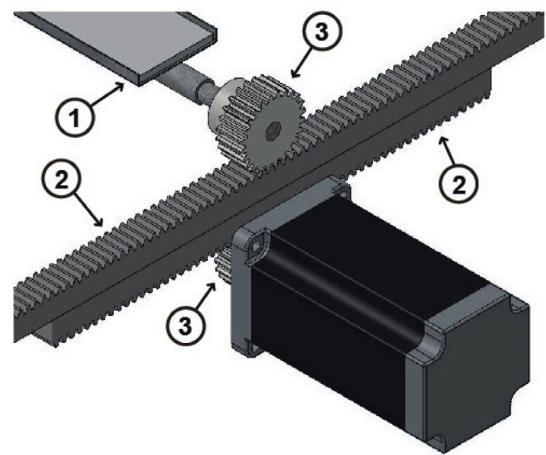


Fig. 6. Overall design of the mirrors movement transmission system.

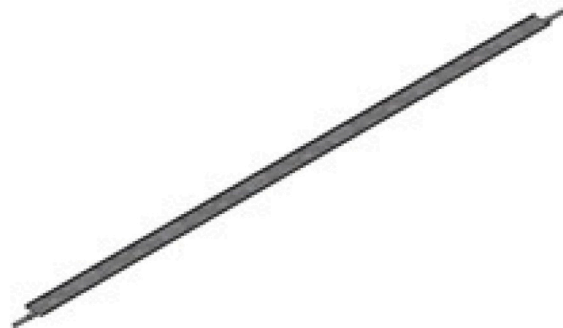


Fig. 7. Overall design of movement unit.

3.2. Mobile structure movement transmission systems

The mobile structure (MS) (1) can be rotated on the east–west axis (See Fig. 8). For this purpose, we used a pinion (2) gear mechanism. This movement requires one movement unit (3).

The movement unit has been designed with SolidWork and includes: two bearings, two bearing supports, two shafts, and two pinion gears [44]. The selected elements are as follows: a standard bearing type FAG6301ZZ, a standard pinion gear with 24 teeth, module 2 (mm) and 35 (mm) thick, a bearing support that consists of a 82.5 (mm) diameter stainless steel tube with a wall 20 (mm) thick, and a $78 \times 28 \times 5$ (mm) stainless steel plate and a shaft that consists of a 25 (mm) diameter carbon steel rod 150 (mm) long.

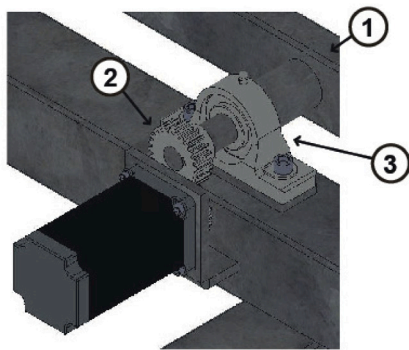


Fig. 8. Overall design of the *MS* movement transmission systems.

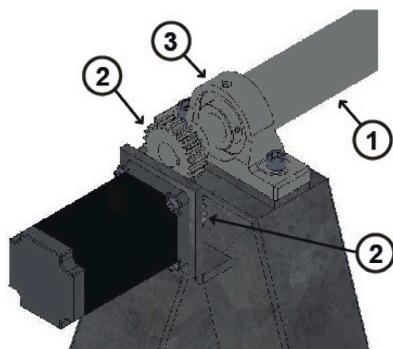


Fig. 9. Overall design of the *SRS* movement transmission system.

Table 1
Sun position for a tracking system algorithms.

Algorithm	Maximum error
International Solar Position Algorithm (<i>SPA</i>) [45]	0.0003°
Michalsky et al. [46]	0.01°
Blanco et al. [47]	0.008°
Grena Algorithm [48]	0.0027°

3.3. Secondary reflector movement transmission systems

The secondary reflector system (*SRS*) can also be rotated on the east–west axis. For this aim, we used a pinion gear mechanism (See Fig. 9). This movement requires one movement unit.

The movement unit has been designed with SolidWorks and it includes: two bearings, two bearing supports, two shafts and two pinion gears [44]. The selected elements are as follows: a standard bearing type *FAG6301ZZ*, a standard pinion gear with 24 teeth, module 2 (mm) and 31 (mm) thick, a bearing support that consists of a 82.5 (mm) diameter stainless steel tube with a wall 20 (mm) thick, and a 78 × 28 × 5 (mm) stainless steel plate and a shaft that consists of a 25 (mm) diameter carbon steel rod 150 (mm) long.

3.4. Stepper motors and drivers

The Sun position for a tracking system can be calculated using different algorithms. Table 1 shows some of these algorithms and its accuracy.

For solar engineering applications the error of the *SPA* is extremely small. For this reason, other authors propose algorithms with greater errors (See Table 2). Taking into account the precision required for this tracking system, it is considered that a stepper motor is the suitable electric motor [49,50]. Therefore, we used stepper motors and its drivers, with a step of 0.006°. The calculations of the necessary torque

Table 2
Cost of the solar tracking system.

Item	Unit cost (€)	Quantity	Cost (€)
Raspberry Pi 3	39.95	1	39.95
Arduino Mini Pro	3.21	4	12.84
XBee module S1	16.95	5	84.75
<i>GPS</i> module	13.95	1	13.95
Laser sensor	23.61	3	70.83
Micro SD Card + Adapter	5.19	1	5.19
Power supply	36	1	36
<i>ULN2083</i> integrated circuit	2	1	2
Thermocouple type <i>K</i> + <i>MAX6675A/D</i>	2.5	2	5
<i>BC639</i> transistor	2.92	1	2.92
Light sensor (<i>VEML7700</i>)	2.95	1	2.95
Limit switch	8.15	5	40.75
4K7 resistor	0.16	10	1.60
7K5 resistor	0.1	4	0.4
10K resistor	0.1	11	1.1
0.33 μF capacitor	0.5	1	0.5
0.1 μF capacitor	0.8	3	2.4
<i>PCB</i> cost	10	5	50
Total			373.13

of the motors has been made with the software SolidWorks [43]. Each driver supplies appropriate control signals and supply voltage to the associated stepper motor.

3.5. Electronic control system

The movements of the *SSLFR* have been controlled by means of an electronic control system. This system consists of several printed circuit board (*PCB*): Master *PCB*, *GPS PCB*, Temperature *PCB*, Position *PCB* and Irradiance *PCB*. The electronic control system was controlled by a master controller (Raspberry pi 3) and supported by 4 slave microcontrollers (Arduino). Figs. 10(a) and Fig. 10(b) show a overall photographs of the electronic control system. Fig. 11 shows a block diagram of the electronic control system for the solar tracking system.

3.5.1. Master PCB

The master *PCB* is implemented with: a Raspberry Pi 3, a Xbee module and two *ULN2083A* integrated circuits. Fig. 12(a) shows a photograph of the Master *PCB*. The Raspberry Pi 3 is used as master controller in the tracking system. This controller has been already used by other authors in similar works [51,52], due to its low cost, compact size, compatibility and easy interfacing. The Raspberry Pi 3 is a single board computer based on a 900MHz quad-core ARM Cortex-A7 CPU, with 1 GB RAM, 40 GPIO pins, 4 USB ports, Full HDMI port, Ethernet port, and a Micro SD card slot [53]. The Raspberry Pi 3 has been used as master controller to perform system algorithms, arithmetic calculation and database generation of the Sun's path. A wireless system has been developed with the help of *XBee* modules. The *XBee* module is a technology for wireless communication among multiple devices in a Wireless Personal Area Network. *XBee* modules are embedded solutions that provide wireless end-point connectivity to devices. This module is a standard for wireless communication based on the *IEEE802.15.4* protocol. The *XBee* module is equipped with an on-chip antenna provided by Digi-MaxStream [54]. The Xbee module has been used to set communication between the Raspberry Pi 3 and the rest of the *PCBs*. The Xbee of the Master *PCB* communicates with the Raspberry Pi 3 via serial *UART* communication protocol. The information of the *PCBs* was received by the Raspberry Pi 3 via the four wired *I2C* communication protocol. The output voltage of the Raspberry Pi is 3.3 (V), and the input voltage of the stepper motor drivers is 5 (V). Therefore, it is necessary to raise the voltage. In order to raise it, an *ULN2083A* integrated circuit is used. The *ULN2083A* device is a 50 (V), 500 (mA) Darlington transistor array [55]. The system

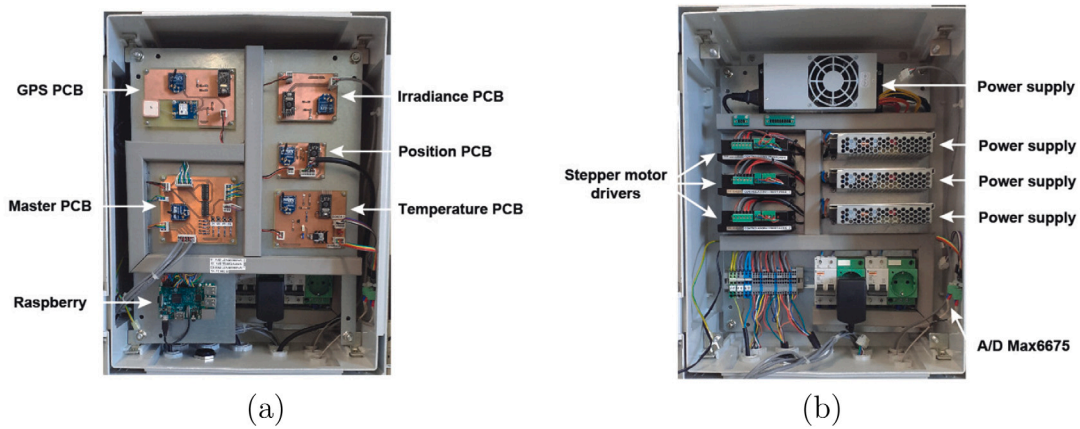


Fig. 10. Overall photographs of the electronic control system.

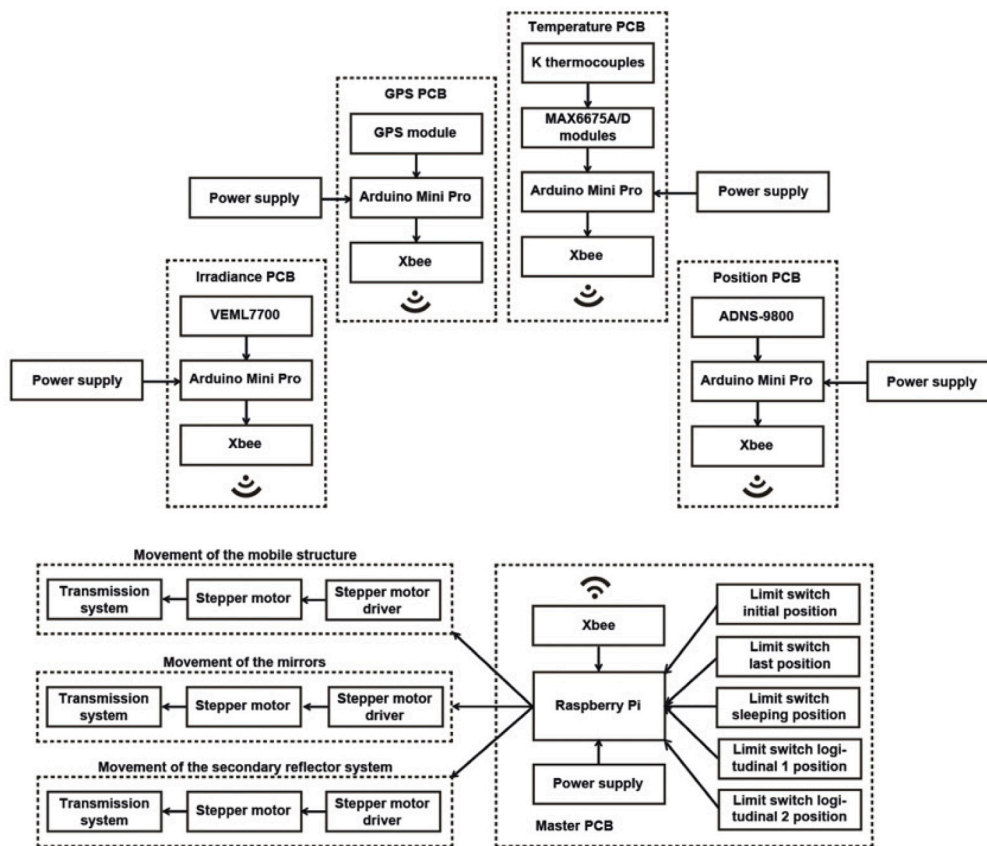


Fig. 11. Block diagram of the electronic control system for the solar tracking system.

uses five limit switches to determine: initial position, last position, sleeping position, longitudinal 1 position and longitudinal 2 position. Its features are: power supply $V_{AC\ max} = 250$ (V), current supply $I_{max} = 15$ (A).

3.5.2. GPS PCB

A *GPS* module has been used to determine location in a standard longitude and latitude coordination system via multiple orbiting satellites [37]. It also provides information about date and *UTC* time. The *GPS PCB* is implemented with: a *GPS* module, an *Arduino Mini Pro*, and a *Xbee* module. Fig. 12(b) shows a photograph of the *GPS PCB*. The *Arduino Mini Pro* microcontroller has been used as an interface with *GPS* module. This takes the data, processes them and sends them to the *Xbee* module for later transmission to the *Raspberry Pi* 3.

The *Arduino Mini Pro* is used because of its low cost, compact size, compatibility and easy interfacing. The *Arduino Mini Pro* is a small microcontroller board based on the *ATmega 328*. It has 14 digital input/output pins (6 of which can be used as *PWM* outputs), 8 analog inputs and a 16 (MHz) crystal oscillator. It can be programmed using the *USB Serial* adapter or another *USB* or *RS232* to *TTL* serial adapter [56]. A *GY-GPS6MV2* [57] has been chosen as *GPS* module.

3.5.3. Temperature PCB

The temperature *PCB* is responsible for reading the input and output temperature values of the absorber tube. It uses two thermocouples to check that the temperature of the absorber tube maintains itself in the stipulated safety range. In our case the maximum temperature value is 150 (°C). In the case this value is exceeded, the mirrors would move

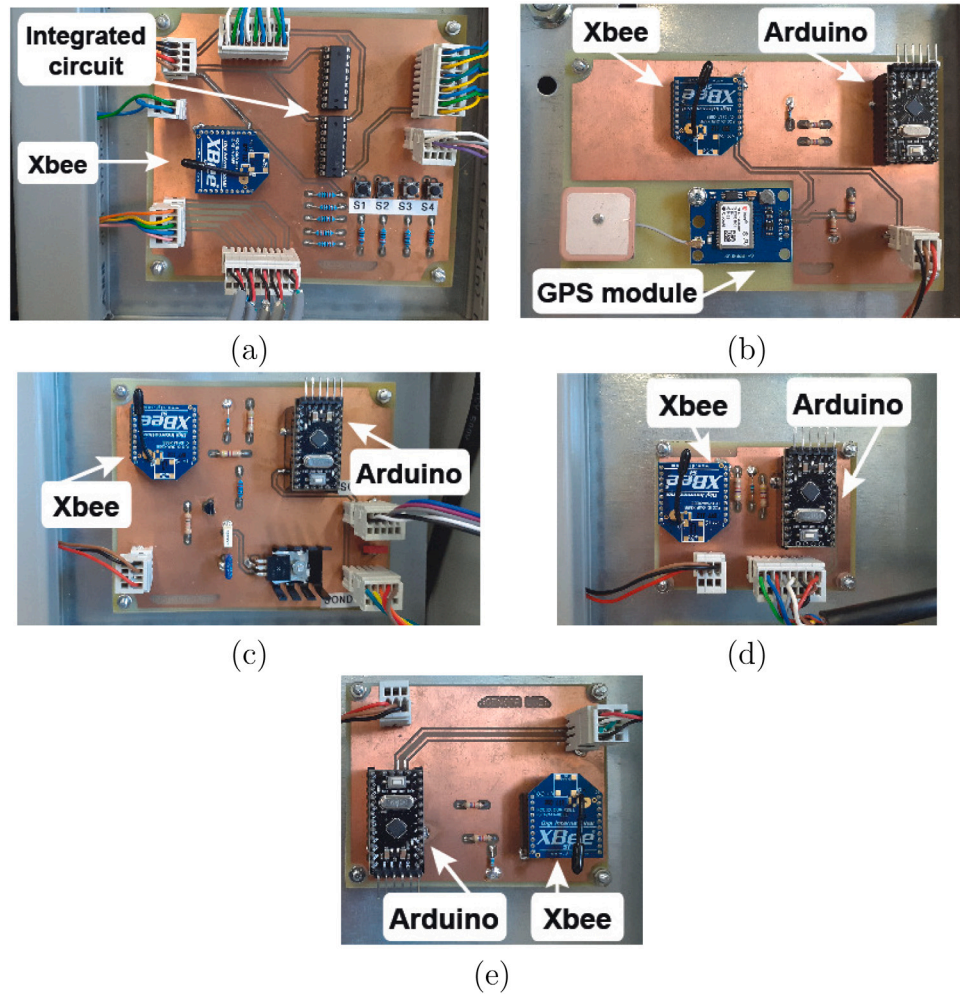


Fig. 12. Photographs of the PCBs.

to the sleeping position. The Temperature *PCB* is implemented with: two thermocouples, two analogues of digital converters, an Arduino Mini Pro and a Xbee module. Fig. 12(c) shows a photograph of the Temperature *PCB*. The Arduino Mini Pro microcontroller has been used to take the data provided by the thermocouples, process them and send them to the Xbee module for later transmission to the Raspberry Pi 3. The thermocouple used is the type-*K* thermocouple [58]. The analogue to digital converter used is the *MAX6675A/D* module [58].

3.5.4. Position *PCB*

The Position *PCB* has been used to assist the Master *PCB* by independently controlling the angular position of mirrors, mobile structure, and the secondary reflector system. The Position *PCB* is implemented with: three laser sensors, three analogues of digital converters, an Arduino Mini Pro and a Xbee module. Fig. 12(d) shows a photograph of the Position *PCB*. The laser sensor used is the *ADNS-9800* [59].

The *ADNS-9800* LaserStream gaming sensor includes a sensor and a *VCSEL* in a single chip-on-board (*COB*) package. The Arduino Mini Pro reads the information from the sensor serial port.

3.5.5. Irradiance *PCB*

The Irradiance *PCB* has been used to assist the Master *PCB* by informing it about the beam solar irradiance. The relationship between illuminance and solar irradiance is 104 (lm/W): its accuracy has been evaluated in [60]. It has been used by other authors [6,61]. The Irradiance *PCB* is implemented with: a light sensor, an Arduino Mini Pro and a Xbee module. Fig. 12(e) shows a photograph of the Irradiance

PCB. The light sensor used is the *VEML7700* [62]. The *VEML7700* is a high accuracy ambient light with a 16-bit resolution and supports an easy to use *I2C* bus communication interface. The ambient light range is 0 to 120.000 (lx) and the ambient light resolution is 0.0036 (lx).

3.6. Cost analysis

The total cost of the implemented solar tracking system is calculated and presented in Table 2. This cost estimation has been conducted according to the local market prices.

4. Solar tracking system algorithm

The solar tracking algorithm has been developed in order to determine the Sun path characteristics such as sunrise, sunset, etc. with high precision for any location year-round.

The mirrors of the primary reflector system can be rotated with one freedom movement (see Fig. 13). This movement in the east-west direction is provided by the stepper motor and its driver. The stepper motor is used to rotate the mirrors of the primary reflector system in both clockwise and counter-clockwise direction with a 360° full rotation. The rotation of the motor goes from -45° to +90° to track the transversal incidence angle. The sunrise matches with $\beta_0 = -45^\circ$. The sunset matches with $\beta_0 = +45^\circ$. The position $\beta_0 = +90^\circ$ is called sleeping position. In this position no dust is deposited on the mirrors.

The mobile structure (*MS*) can be rotated with one freedom movement (see Fig. 14). This movement in the north-south direction is

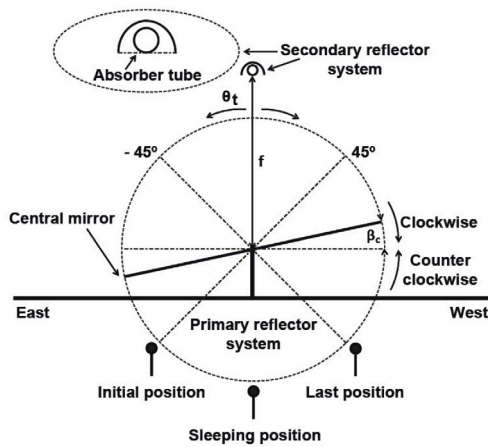


Fig. 13. Movement of the central mirror.

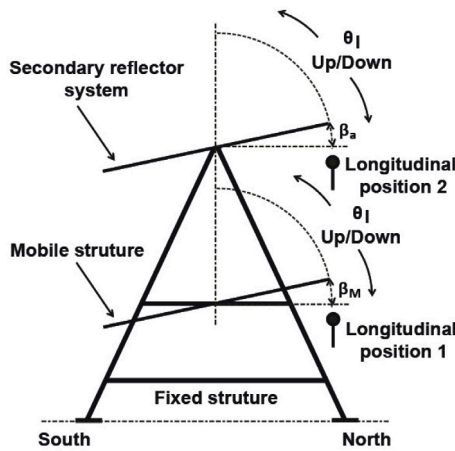


Fig. 14. Movement of the MS and SRS.

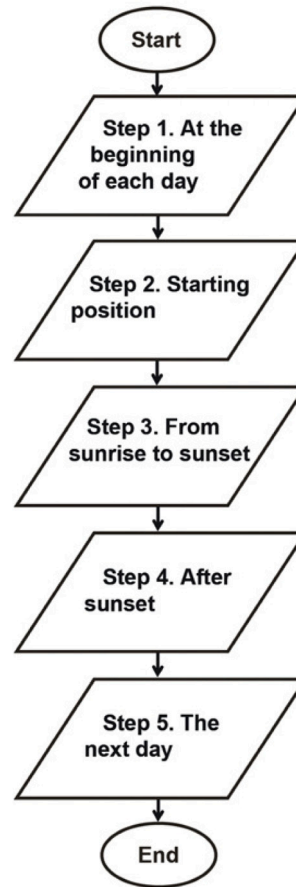


Fig. 15. Algorithm flow chart.

provided by the stepper motor and its driver. The stepper motor is used to tilt the mobile structure up and down for tracking the zenith angle. Its rotation varies from 0° to 90° to track the zenith angle of the Sun.

The secondary reflector system (SRS) can also be rotated with one freedom movement (see Fig. 14). This movement in the north–south direction is provided by the stepper motor and its driver. The stepper motor is used to tilt the secondary reflector system up and down to track the zenith angle. This rotation goes from 0° to 90° .

The calculation has been made following five steps. In the first step the solar angles have been determined using solar time, geographical latitude and other parameters such as daily angle, declination angle, and hour angle. In the second step, the solar angles have been used to determine the transversal and the longitudinal incidence angles. Then, in the next steps, all the SSLFR movements have been determined. Fig. 15 shows the flow chart of the tracking system algorithm.

4.1. Step 1. At the break of dawn

Fig. 16 shows the algorithm flow chart for the Step 1.

(1.1) During the initialization of the system, at the break of dawn, it is necessary to get important information such as date, solar time and precise longitude and latitude for the SSLFR's specific location. This information can be obtained by using a GPS module.

(1.2) The system does some mathematical calculations [20] based on the information obtained from the GPS module, to get the sunrise and sunset time, the Sun's position, the transversal and longitudinal

incidence angles, the tilt of the central mirror, the tilt of the mobile structure and the tilt of the secondary reflector system, for each second of the day. These values are tabulated in a database. The database is set for the daily tracking.

(1.3) The tracking system automatically aligns the mirrors, the mobile structure, and the secondary reflector system using the information from the tabulated database.

The generated database consists of: (i) seconds of the day, (ii) transversal movement steps, (iii) longitudinal one-movement steps, (iv) longitudinal two-movements steps, (v) longitudinal one-movement direction, (vi) longitudinal two-movements direction. The database matrix has 86400 vectors (one for each second of the day) and 6 different variables, with a total of 518.400 values. It takes approximately 8 seconds to generate the database. The mirrors' track speed is 0.006 ($^\circ$) per second.

4.2. Step 2. Starting position

Fig. 17 shows the algorithm flow chart for the Step 2. Before sunrise, the transversal motion control rotates all the mirror in counter clockwise up from the sleeping position to the initial position (sunrise) (See Fig. 13).

In the starting position it has been considered that: (i) The mirrors are located in the initial position; (ii) The mobile structure is located in the longitudinal position 1 and (iii) The secondary reflector system is located in the longitudinal position 2.

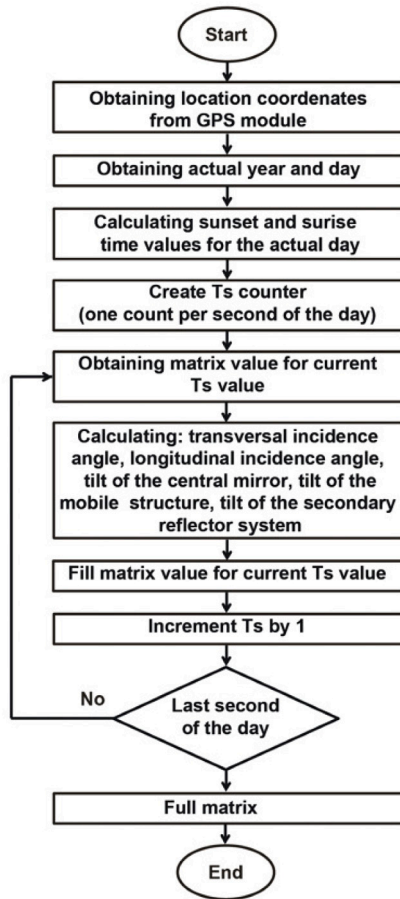


Fig. 16. Step 1 algorithm flow chart.

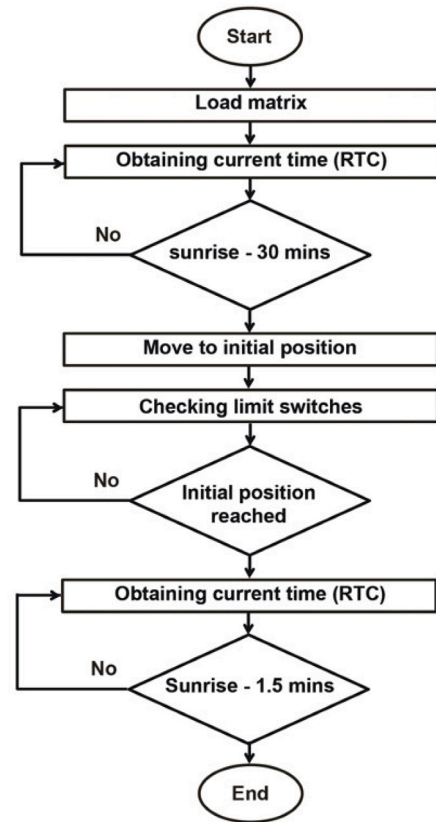


Fig. 17. Step 2 algorithm flow chart.

4.3. Step 3. From sunrise to sunset

Fig. 18 shows the algorithm flow chart for the Step 3. This is the step in which the solar path is followed by the mirrors basing on the information from the tabulated database.

The following events occur at the same time:

(3.1) The transversal motion control rotates the mirrors in clockwise up from the initial position (sunrise) to the last position (sunset) (See Fig. 13).

(3.2) The motor moves the mobile structure up from longitudinal position 1 (sunrise) until noon and brings it back to its original position at sunset (See Fig. 14) in order to control the longitudinal motion of the mobile structure.

(3.3) The motor moves the secondary reflector system up from longitudinal position 2 (sunrise) until noon and brings the secondary reflector system back to its original position at sunset (See Fig. 14). In order to control the longitudinal motion of the secondary reflector system.

All of the referred motions follow the tracking path generated at the beginning of the day with the database.

4.4. Step 4. After sunset

Fig. 19 shows the algorithm flow chart for the Step 4.

(4.1) The transversal motion control rotates the mirrors in clockwise up from last position (sunset) to the sleeping position (See Fig. 13).

(4.2) Then, the electronic system goes into a sleeping mode in order to reduce the power consumption. In addition, the sleeping position avoids any dust particle or other elements being deposited on the mirrors.

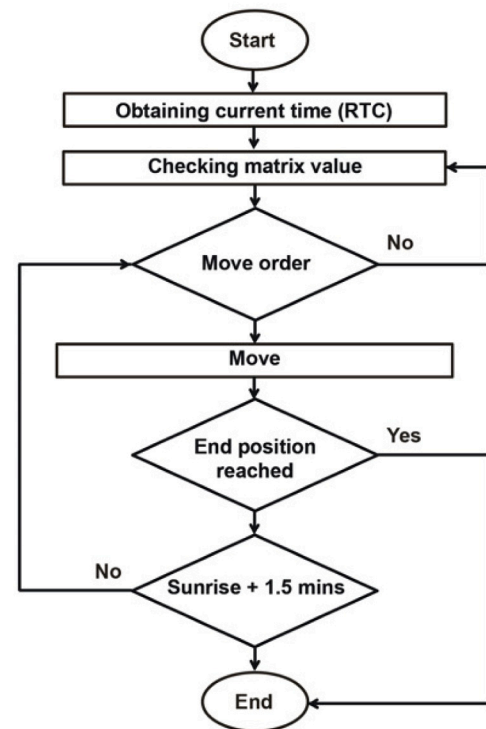


Fig. 18. Step 3 algorithm flow chart.

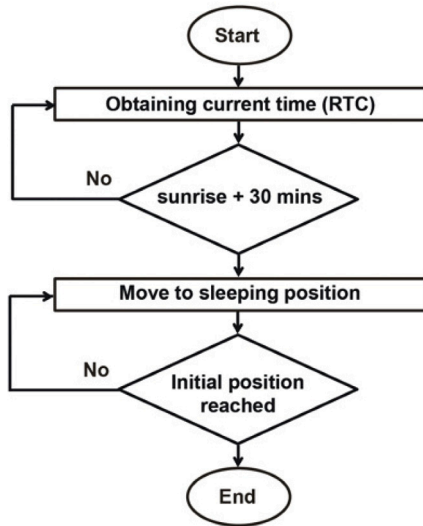


Fig. 19. Step 4 algorithm flow chart.

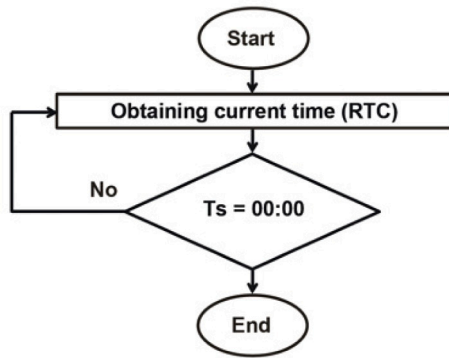


Fig. 20. Step 5 algorithm flow chart.

4.5. Step 5. The next day

Fig. 20 shows the algorithm flow chart for the Step 5. At 0:00 all the process starts again from step 1.

5. Result and discussion

The aims of this section are: (1) to estimate the effects of the tracking error on the power absorbed by the absorber tube, (2) to estimate the effects of the proposed tracking system on the total annual energy absorbed by the absorber tube, (3) to estimate the effects of the proposed tracking system on the energy-to-area ratio and (4) to estimate the effects of the proposed tracking system on the levelized cost of energy. These parameters affect the performance of small scale linear Fresnel reflectors.

In order to carry out this study, a specific software has been developed in *MATLAB* code. All the calculations are based on a sub-hourly distribution of the direct normal irradiance for the specific geographic location. DNI is obtained from a satellite database. We have used *PVGIS* [63] to obtain monthly averages of its value per day. We transform these averages into a continuous distribution of beam solar irradiance by means of Fourier Series, as shown in [64]. We do not need to consider shadowing or blocking because our design has already covered these issues [65].

Table 3
SSLFR parameters constants used in the study.

Parameters	Value	References
n	Number of mirrors at each side of the central mirror	12 [14,23]
W_M	Mirror width	0.06 (m) [14,23,22]
L_M	Mirror length	2.00 (m) [14,23]
d	Separation between two consecutive mirrors	0.024 (m) [14,23]
D	Diameter of the absorber tube	0.0486 (m) [14,23]
f	Height of the receiver	1.50 (m) [14,23,21,22]
L_a	Length of the absorber tube	2.00 (m) [14,23]
ρ	Reflectivity of the mirrors	0.94 [42]
CL_m	Cleanliness factors of the mirror	0.96 [66]
CL_g	Cleanliness factors of the glass covering the secondary absorber	0.96 [66]
τ	Transmissivity of the glass	
	if $\alpha_i \leq 20^\circ$	0.87 [67]
	if $20^\circ \leq \alpha_i \leq 30^\circ$	0.85 [67]
α_b	Absorptivity of the absorber tube	0.95 [68]

5.1. Case study

We have considered a specific geographic location: Almeria (Spain), with latitude $36^\circ 50' 07''$ N, longitude $02^\circ 24' 08''$ W and altitude 22 (m). We have also considered a specific SSLFR. The SSLFR parameters listed in Table 3 remain constant throughout all the study. Although the study focuses on a specific location and on a certain SSLFR, it can be extended to other locations and other SSLFR parameters.

Numerical simulations have been carried out and compared with the configuration used in large-scale LFRs. In large-scale LFRs the mirrors and the absorber tube form a longitudinal angle of 0° with the horizontal plane ($\beta_M = \beta_a = 0^\circ$). The parameters of the absorber tube, left length of the single absorber tube (L_a^l) and right length of the single absorber tube (L_a^r), are different to the configuration used in large-scale LFRs and the proposed tracking system. For the configuration used in large-scale LFRs, these parameters are: $L_a^l = -0.037$ (m), $L_a^r = -2.037$ (m) [14]. For the proposed tracking system, the parameters of the studied case are [24]: $L_a^l = 1.005$ (m) and $L_a^r = -1.005$ (m). (According to the sign convention that we have adopted: lengths from the center of the mirror to the left are considered positive and those to the right, negative).

5.2. Effects the tracking error on the power absorbed by the absorber tube

The tracking error is usually defined as the standard deviation of the error between the actual and the ideal position of the mirrors. This deviation can be caused by systematic errors like: errors in the calculation of the Sun position, geo-positioning error, transmission system error, errors in the orientation of the SSLFR, etc. The SSLFR is considered to be perfectly aligned in a North–South orientation.

In order to simplify the exposition, we shall only consider a solar tracking error $\epsilon > 0$ (in radians) such that:

$$\beta_i^e = \beta_i - \epsilon \tag{17}$$

for both, the mirrors on the left and those on the right, where β_i^e ($^\circ$) is the tilt angle of i th mirror under solar tracking error. As the mirrors have all the same angular velocity, all of them fall into the same error. Barbón et al. [65] have introduced a relationship for computing the tracking error of a small-scale linear Fresnel reflector. A brief description is supplied here (complete details are provided in [65]). The power Q absorbed by the absorber tube, in an SSLFR with receiver

cavity in the shape of an involute is [65]:

$$Q = \begin{cases} \sum_{i=1}^{2n+1} DNI \cdot \eta_{opt} \cdot l_{abs} \cdot W_M \cdot \cos \theta_i & \text{if } W_{ai} \cdot \cos \alpha_i < D \\ \sum_{i=1}^{2n+1} DNI \cdot \eta_{opt} \cdot l_{abs} \cdot D & \text{if } W_{ai} \cdot \cos \alpha_i = D \\ \sum_{i=1}^{2n+1} DNI \cdot \eta_{opt} \cdot l_{abs} \cdot (D + l_{cr} \cdot \rho_{rc}) & \text{if } W_{ai} \cdot \cos \alpha_i > D \end{cases} \quad (18)$$

where DNI is the direct normal irradiance (W/m^2), η_{opt} is the total optical yield (dimensionless), l_{abs} is the longitudinal length of the absorber tube which is illuminated (m), W_M is the mirror width (m), D is the diameter of the absorber tube (m), θ_i is the angle between the normal to the mirror and the incidence of the Sun ray ($^\circ$), W_{ai} is the width of the absorber tube illuminated by the i th mirror (m), α_i is the angle between the vertical at the focal point and the line connecting the center point of each mirror to the focal point ($^\circ$), l_{cr} is the length of rays falling indirectly on the absorber tube (m), ρ_{rc} is the reflectivity of the rays falling indirectly on the absorber tube (dimensionless) and n is the number of mirrors at each side of the central mirror. η_{opt} can be calculated with:

$$\eta_{opt} = \rho \cdot CI_m \cdot CI_g \cdot \tau \cdot \alpha_b \quad (19)$$

where ρ is the reflectivity of the mirrors, CI_m is the cleanliness factors of the mirror, CI_g is the cleanliness factors of the glass covering of the secondary reflector system, τ is the transmissivity of this glass, and α_b is the absorptivity of the absorber tube.

Let us make some preliminary considerations on the dependence of some elements of Eq. (18) related to the tracking error: (i) The DNI is not affected by tracking errors; (ii) Concerning with η_{opt} , although some of its constituent parameters (mainly τ) change with the angle of incidence (see [42]), we consider them to be constant for simplicity (see [69,70]) and (iii) The parameter l_{abs} is constant, as we are only performing a transversal study.

Fig. 21 shows the power absorbed by each mirror of the absorber tube, for Spring equinox, Summer solstice, Autumn equinox and Winter solstice. In this figure, the label 12L reports the power absorbed due to the 12th left mirror, the label C reports the power absorbed due to central mirror, and the label 12R reports the power absorbed due to the 12th right mirror. There we can see that the power absorbed in case of no error is symmetrical, as it can theoretically be deduced. For example, the power of the 12L mirror at 9:00 is equal to that of 12R mirror at 15:00 and it is also obvious that at 12:00 the power of the 12L mirror is equal to that of the 12R.

The impact of the tracking error on the power absorbed by the absorber tube can be estimated using the equation [65], given by:

$$Q^e = \begin{cases} \sum_{i=1}^{2n+1} DNI \cdot \eta_{opt} \cdot l_{abs} \cdot W_M \cdot \cos \theta_i^e & \text{if } [r_i, l_i] \in [-D/2, D/2] \\ \sum_{i=1}^{2n+1} DNI \cdot \eta_{opt} \cdot l_{abs} \cdot [(b_i - a_i) + l_{cr}^e \cdot \rho_{rc}] & \text{if } [r_i, l_i] \notin [-D/2, D/2] \end{cases} \quad (20)$$

with:

$$[r_i, l_i] = [- (W_{ai}^e/2 + \overline{OO'}) \cdot \cos \alpha_i^e, (W_{ai}^e/2 - \overline{OO'}) \cdot \cos \alpha_i^e]; \quad 1 \leq i \leq 2n+1 \quad (21)$$

$$[a_i, b_i] = [r_i, l_i] \cap [-D/2, D/2]; \quad 1 \leq i \leq 2n+1 \quad (22)$$

$$l_{cr}^e = (l_i - r_i) - (b_i - a_i); \quad 1 \leq i \leq 2n+1 \quad (23)$$

where DNI is the direct normal irradiance (W/m^2), η_{opt} is the total optical yield (dimensionless), l_{abs} is the longitudinal length of the absorber tube which is illuminated (m), W_M is the mirror width (m), D is the diameter of the absorber tube (m), θ_i^e is the angle between the normal to the mirror and the incidence of the Sun ray with tracking error ($^\circ$), W_{ai}^e is the width of the absorber tube illuminated by the i -th mirror with tracking error (m), α_i^e is the angle between the vertical at the focal point and the line connecting the center point of each mirror to the focal point with tracking error ($^\circ$), l_{cr}^e is the length of rays falling indirectly on the absorber tube with tracking error (m), $\overline{OO'}$ is the displacement of the geometric focal point, ρ_{rc} is the reflectivity of the rays falling indirectly on the absorber tube (dimensionless) and n is the number of mirrors at each side of the central mirror.

It is important to indicate that when a tracking error $\epsilon > 0$, the same for all the mirrors of the *SSLFR*, is introduced, the symmetry shown in Fig. 21 (power in ideal case) now disappears. The reason for this fact is that the most important effect of the solar tracking error is the displacement of the geometric focal point. As this focal point is always displaced to the right side, then the symmetry between the right and the left area of the *SSLFR* disappears.

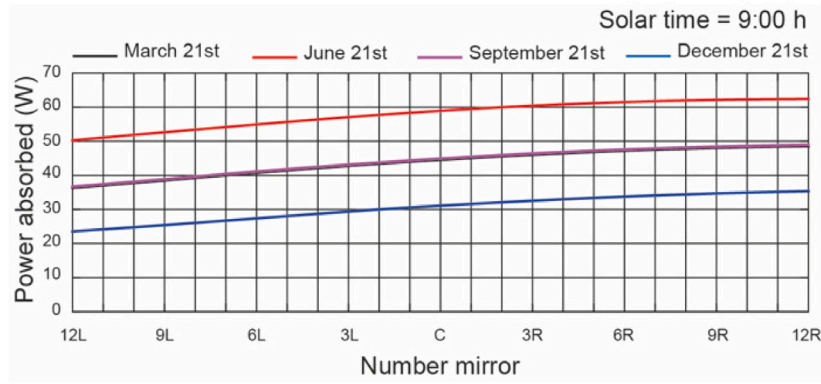
The power absorbed by the absorber tube with tracking error is normalized according to the correct tracking. For this purpose, we shall compute the difference between the power absorbed under tracking error (Q^e) and that absorbed in the ideal case (Q). These values are % of power loss, related to the ideal case, this is its relationship:

$$Power\ loss = \frac{Q - Q^e}{Q} \times 100 \quad (24)$$

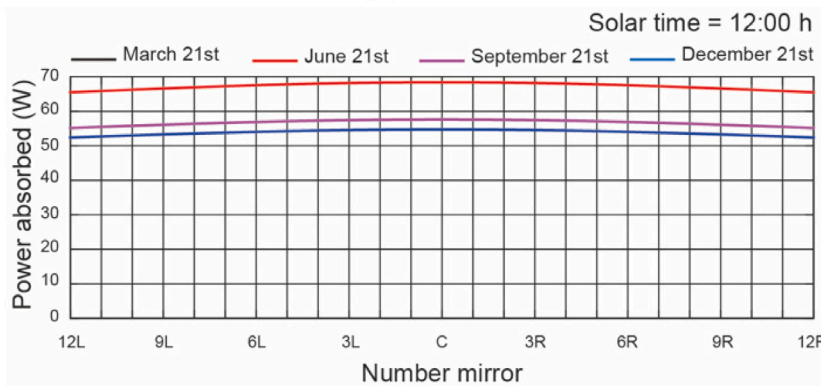
The analysis has been carried out introducing five different tracking errors (0.03 ($^\circ$), 0.06 ($^\circ$), 0.12 ($^\circ$), 0.24 ($^\circ$) and 0.36 ($^\circ$)) over the 25 mirrors which compose the primary reflector system. Different days of the year, times of day and position of the mirrors will be analyzed. The analyzed days of the year are: Spring equinox (March 21st), Summer solstice (June 21st), Autumn equinox (September 21st) and Winter solstice (December 21st). The analyzed hours of the day are: 9:00, 12:00 and 15:00. Now the plots are not symmetrical.

Figs. 22–24 shows the effects of tracking errors on different mirrors, for Spring equinox, Summer solstice, Autumn equinox, and Winter solstice. The color map in each day shows the mirrors. In these figures, the label 12L reports the power loss (see Eq. (24)) due to the 12th left mirror, the label C reports the power loss due to central mirror, and the label 12R reports the power loss due to the 12th right mirror.

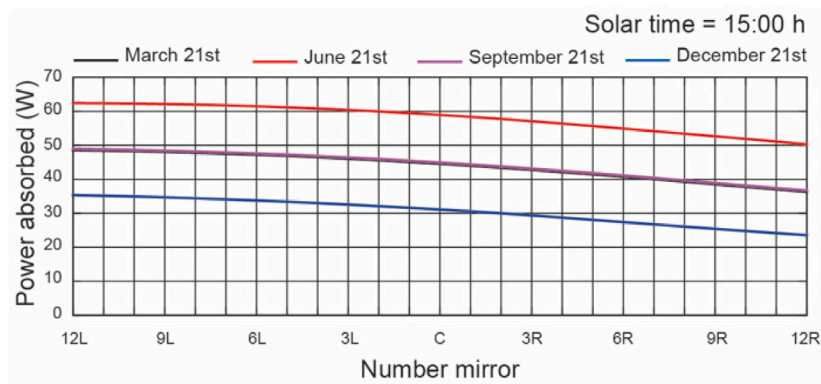
For each mirror, the influence of increasing tracking error is different for each studied day. The tracking error influence is bigger on the mirrors as they get further away from the central mirror. The hours of the day at which the influence of the tracking error is bigger are the hours furthest from of the noon. Generally, the day of the year in which tracking error is smaller is the Summer solstice. The histograms show that tracking systems with a maximum tracking error of 0.03 ($^\circ$) collect 100% of the theoretical value for all mirrors at 12:00, about 99.7% at 9:00 and 15:00. The algorithm proposed for [45,47,48,46] can be used every day of the year without reducing the power absorbed by the absorber tube. The histograms show that tracking systems with a maximum tracking error of 0.06 ($^\circ$) collect 100% of the theoretical value for all mirrors at 12:00, about 99.2% at 9:00 and 15:00. The histograms show that tracking systems with a maximum tracking error of 0.12 ($^\circ$) collect about 99.7% of the theoretical value for all mirrors at 12:00, about 99.0% at 9:00 and 15:00. The histograms show that tracking systems with a maximum tracking error of 0.24 ($^\circ$) collect about 98.5% of the theoretical value for all mirrors at 12:00, about 97.3% at 9:00 and 15:00. The histograms show that tracking systems with a maximum tracking error of 0.36 ($^\circ$) collect about 97.4% of the theoretical value for all mirrors at 12:00, about 96.5% at 9:00 and 15:00.



(a) 9:00



(b) 12:00



(c) 15:00

Fig. 21. Power absorbed by the absorber tube in ideal case.

5.3. Effects of the proposed tracking system on the total annual energy absorbed by the absorber tube

The total annual energy absorbed by the absorber tube (E) can be calculated from Eq. (18). E can be calculated with the following equation

$$E = \sum_{n_d=1}^{365} \left[\int_0^{24} Q_{n_d} dT_S \right] \quad (25)$$

where E is the total annual energy absorbed by the absorber tube (MWh), Q is the power absorbed by the absorber tube (MW), T_S is the solar time, and n_d is the ordinal of the day.

Considering the configuration used in large-scale LFRs and the proposed tracking system, the results obtained are: $E = 8.17$ (MWh) and $E = 9.53$ (MWh), respectively. The parameters of the studied case

have been used for both calculations. The energy obtained with the proposed tracking system is 16.64% more than the one obtained with the configuration used in large-scale LFRs.

5.4. Effects the proposed tracking system on the energy-to-area ratio

In some circumstances the surface required for the installation of an SSLFR is a critical parameter in urban applications. Therefore, we will use the parameter energy-to-area ratio (EAR). The EAR can be calculated from the equation:

$$EAR = \frac{E}{A} \quad (26)$$

where E is the total annual energy absorbed by the absorber tube (MWh) and A is the area required for the SSLFR installation (m^2).

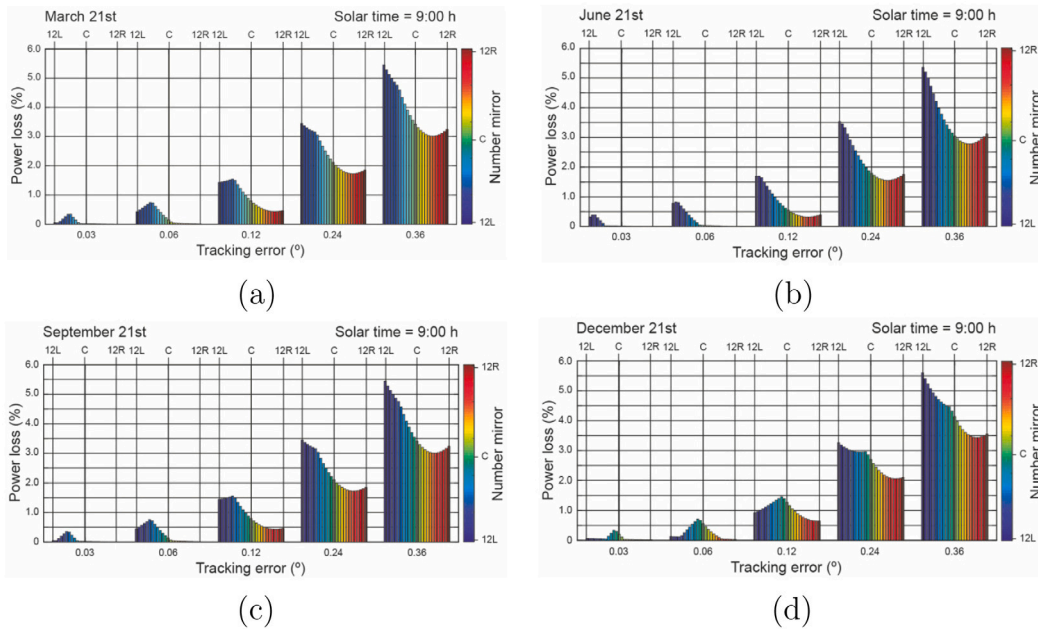


Fig. 22. Power absorbed by the absorber tube with tracking error at 9:00.

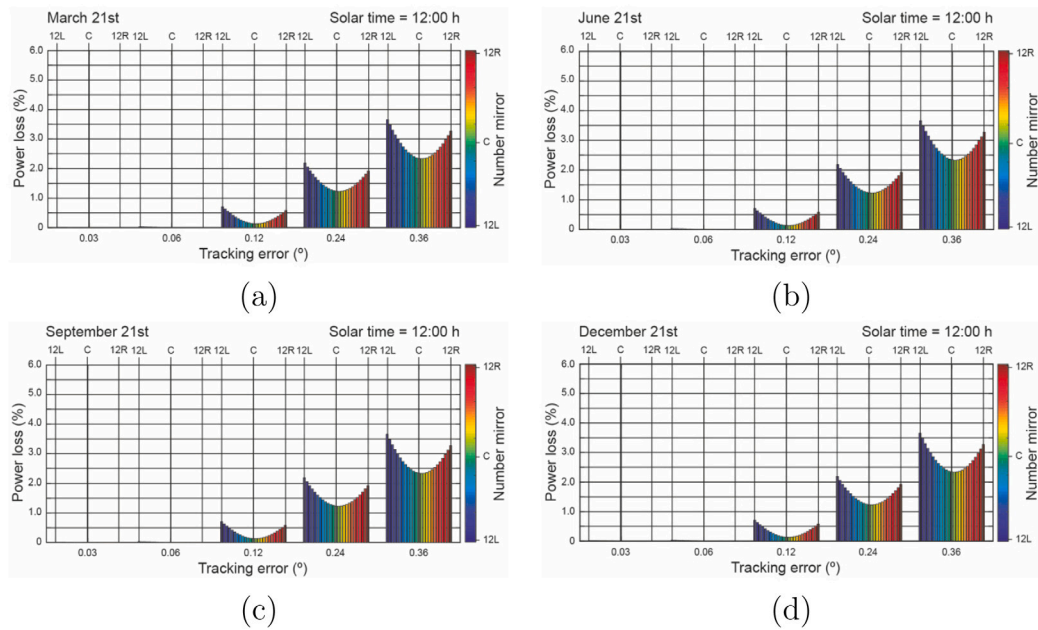


Fig. 23. Power absorbed by the absorber tube with tracking error at 12:00.

The A can be calculated from the equation:

$$A = W \cdot L \tag{27}$$

where W is the mirror field width, and L is the reflector length. The mirror field width can be calculated from the equation (see Fig. 3):

$$W = 2 \cdot n \cdot (W_M + d) + W_M \tag{28}$$

where n is the number of mirrors at each side of the central mirror, W_M is the mirror width (m) and d is the distance between one mirror and its closer one (m). The reflector length L can be calculated with the relations presented in [24]. The formula for L includes: the mirror length L_M (m), the left length of the single absorber tube L'_a (m), the right length of the single absorber tube L''_a (m), the angle between the mirror axis and the horizontal plane β_M (°), and the angle between the

absorber tube and the horizontal plane β_a (°). The optimal choice of values L'_a and L''_a had already been studied in detail in [14].

Considering the configuration used in large-scale LFRs and the proposed tracking system, the results obtained are: $EAR = 1.30$ (MWh/m²) and $EAR=2.32$ (MWh/m²), respectively. The energy-to-area ratio obtained with the proposed tracking system is 78.46% more than the one obtained with the configuration used in large-scale LFRs.

5.5. Effects the proposed tracking system on the levelized cost of energy

There are several levelized cost of energy (LCOE) models for determining renewable energy prices [71]. The LCOE equation may vary to suit the type of analysis [72]. In this study, we used the equation proposed by [73] which is a modification of the equation proposed by

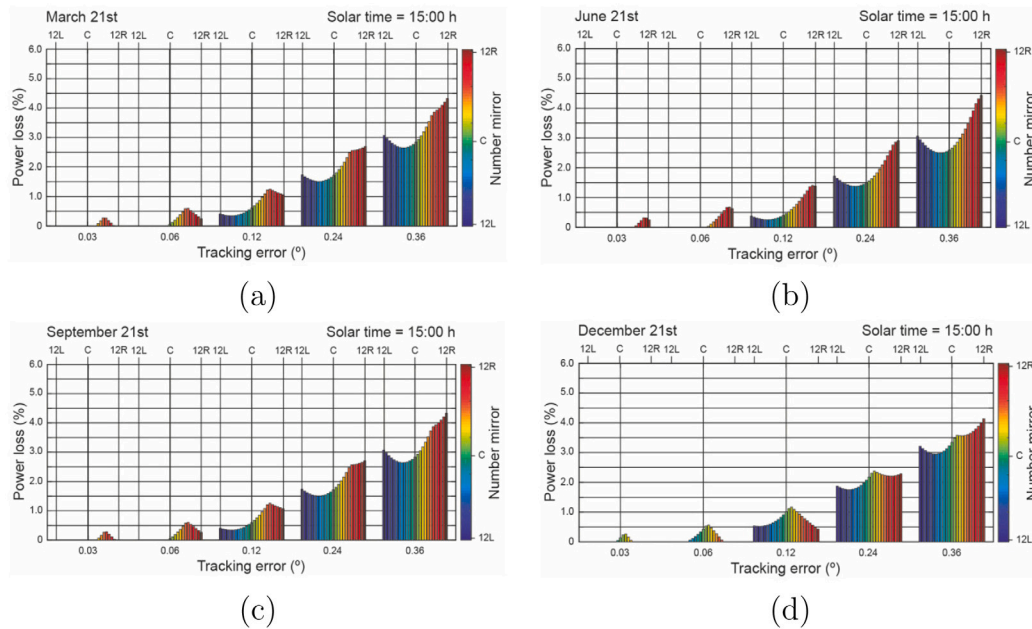


Fig. 24. Power absorbed by the absorber tube with tracking error at 15:00.

IRENA [74]. The $LCOE$ (€/kWh) is estimated by calculating the current value of all the costs incurred during the lifetime of the $SSLFR$ divided by the current value of the total amount of energy absorbed by the absorber tube.

$$LCOE = \frac{\sum_{i=1}^m \frac{DC_i + IC_i + M_i + F_i}{(1+r)^i}}{\sum_{i=1}^m \frac{E_i}{(1+r)^i}} \quad (29)$$

where, DC_i (€) is the direct capital cost in year i , IC_i (€) is the indirect capital cost in year i , M_i (€) is the whole of operations and maintenance expenditures in year i , F_i (€) is the fuel expenditures in year i , m is the expected lifetime of the $SSLFR$, E_i is the energy absorbed by the absorber tube in year i , and r is the real discount rate.

The direct capital cost includes the purchase and the installation of the $SSLFR$. The indirect capital cost includes the design and the construction of the rest of the installation. As we are not studying a specific installation, we will only consider the direct capital cost. As a reasonable expectation of $SSLFR$ operation and maintenance costs, an annual 0.5% of the direct capital cost is recommended.

The methodology proposed by [44] is applied to obtain the total cost. For a better understanding, its parameters are presented in [44]. The total cost of an $SSLFR$ with the configuration used in large-scale $LFRs$ is $C_T = 5299.53$ (€) whereas with the proposed tracking system it is $C_T = 5865.98$ (€). Considering the configuration used in large-scale $LFRs$ and the proposed tracking system, the results obtained are: $LCOE = 0.65$ (€/kWh) and $LCOE = 0.62$ (€/kWh), respectively. The $LCOE$ obtained with the proposed tracking system is 4.62% lower than the one obtained with the configuration used in large-scale $LFRs$.

6. Conclusions

A solar tracking system for small-scale linear Fresnel reflector with three movements has been designed, fabricated, and simulated in the present work. The system uses an open-loop control. This system is able to position itself automatically using a Sun path algorithm and the Global Positioning System. The control system of the solar tracker is governed by a Raspberry Pi together with other auxiliary devices which include Global Positioning System. The solar tracking system consists of several printed circuit boards: Master, Global Positioning System, Temperature, Position, and Irradiance. The electronic control system consists of a master controller (Raspberry pi 3), 4 slave microcontrollers

(Arduino), Global Positioning System module, thermocouples, laser sensors, transversal positioning sensors and longitudinal positioning sensors. The system performance, in terms of the power absorbed by the tube absorber, has been evaluated by comparing the results obtained by evaluating the small-scale linear Fresnel reflector in the ideal case, with those obtained considering tracking errors. For this purpose, different tracking errors, days of the year, times of day and position of the mirrors have been analyzed. The tracking errors analyzed are: 0.03 (°), 0.06 (°), 0.12 (°), 0.24 (°) and 0.36 (°). The days of the year analyzed are: Spring equinox (March 21st), Summer solstice (June 21st), Autumn equinox (September 21st), and Winter solstice (December 21st). The hours of the day analyzed are: 9:00, 12:00 and 15:00. The total cost of the implemented solar tracking system has been calculated. The following conclusions can be drawn: (i) Tracking error influence gets bigger as the mirrors get further away from the central mirror; (ii) Tracking errors smaller than 0.06 (°) are acceptable (they cause power losses smaller than 1%), whereas errors bigger than 0.36 (°) start being noticeable (power losses greater than 3%); (iii) The low cost solution proposed is presented as a good alternative for the control system of the solar tracker of the small-scale linear Fresnel reflector with three movements; (iv) The hours of the day at which the influence of the tracking error is bigger, are the furthest ones from of the noon; (v) Generally, the day of the year in which the tracking error is smaller is the Summer solstice. Finally, we highlight that the proposed new tracking system gives 16.64% more energy, 78.46% higher energy-to-area ratio, and 4.62% less levelized cost of energy than the classic tracking system with one movement used in large-scale $LFRs$.

CRedit authorship contribution statement

A. Barbón: Conceptualization, Methodology. **J.A. Fernández-Rubiera:** Methodology, Data curation. **L. Martínez-Valledor:** Software, Methodology, Writing - original draft. **A. Pérez-Fernández:** Software, Methodology, Writing - original draft. **L. Bayón:** Conceptualization, Methodology.

Declaration of competing interest

The authors declare that they have no known competing financial interests or personal relationships that could have appeared to influence the work reported in this paper.

Acknowledgments

The authors gratefully acknowledge the financial support from the University of Oviedo, Spain (Ref. PAPI-18-EMERG-31). We wish to thank Dr. Laudino Rodríguez, head of the CIFP-Mantenimiento y Servicios a la Producción vocational training school in La Felguera, Asturias, Spain, for his work of building the prototype for the design presented in this paper.

References

- [1] Rovira A, Barbero R, Montes MJ, Abbas R, Varela F. Analysis and comparison of integrated solar combined cycles using parabolic troughs and linear Fresnel reflectors as concentrating systems. *Appl Energy* 2016;162:990–1000.
- [2] Sebastián A, Abbas R, Valdés M, Casanova MJ. Innovative thermal storage strategies for Fresnel-based concentrating solar plants with East-West orientation. *Appl Energy* 2018;230:983–95.
- [3] Dellicompani P, Franco J. Potential uses of a prototype linear Fresnel concentration system. *Renew Energy* 2019;136:1044–54.
- [4] Singh R. Modeling and performance analysis of linear Fresnel collector for process heat generation for ice cream factory in Konya [MS Thesis], Middle East Technical University; 2017.
- [5] Arteconi A, Del Zotto L, Tascioni R, Cioccolanti L. Modelling system integration of a micro solar organic Rankine cycle plant into a residential building. *Appl Energy* 2019;251:113408.
- [6] Barbón A, Sánchez-Rodríguez JA, Bayón L, Barbón N. Development of a fiber daylighting system based on a small-scale linear Fresnel reflector: Theoretical elements. *Appl Energy* 2018;212:733–45.
- [7] Kincaid N, Mungas G, Kramer N, Wagner M, Zhu G. An optical performance comparison of three concentrating solar power collector designs in linear Fresnel, parabolic trough, and central receiver. *Appl Energy* 2018;231:1109–21.
- [8] Montes MJ, Barbero R, Abbas R, Rovira A. Performance model and thermal comparison of different alternatives for the Fresnel single-tube receiver. *Appl Therm Eng* 2016;104:162–75.
- [9] Balaji S, Reddy KS, Sundararajan T. Optical modelling and performance analysis of a solar LFR receiver system with parabolic and involute secondary reflectors. *Appl Energy* 2016;179:1138–51.
- [10] Grena R, Tarquini P. Solar linear Fresnel collector using molten nitrates as heat transfer fluid. *Energy* 2011;36:1048–56.
- [11] Hack M, Zhu G, Wendelin T. Evaluation and comparison of an adaptive method technique for improved performance of linear Fresnel secondary designs. *Appl Energy* 2017;208:1441–51.
- [12] Moghimi MA, Craig KJ, Meyer JP. Optimization of a trapezoidal cavity absorber for the linear Fresnel reflector. *Sol Energy* 2015;119:343–61.
- [13] Chen F, Li M, Emam Hassanien RH, Luo X, Hong Y, Feng Z, et al. Study on the optical properties of triangular cavity absorber for parabolic trough solar concentrator. *Int J Photoenergy* 2015. Article ID 895946, 9 pages.
- [14] Barbón A, Barbón N, Bayón L, Otero JA. Optimization of the length and position of the absorber tube in small-scale linear Fresnel concentrators. *Renew Energy* 2016;99:986–95.
- [15] Cau G, Cocco D. Comparison of medium-size concentrating solar power plants based on parabolic trough and linear Fresnel collectors. *Energy Procedia* 2014;45:101–10.
- [16] Yanqing Z, Jifu S, Yujian L, Leilei W, Qizhang H, Gang X. Design and experimental investigation of a stretched parabolic linear Fresnel reflector collecting system. *Energy Convers Manage* 2016;126:89–98.
- [17] Morin G, Dersch J, Platzer W, Eck M, Häberle A. Comparison of linear Fresnel and parabolic trough collector power plants. *Sol Energy* 2012;86:1–12.
- [18] Elmaanaoui Y, Saifaoui D. Parametric analysis of end loss efficiency in linear Fresnel reflector. In: International renewable and sustainable energy conference. IEEE; 2014, p. 104–7.
- [19] Dai J, Zheng H, Su Y, Chang Z. The motional design and analysis for linear Fresnel reflector system combined three-movement. *Energy Procedia* 2012;14:971–6.
- [20] Barbón A, Barbón N, Bayón L, Otero JA. Theoretical elements for the design of a small-scale linear Fresnel reflector: Frontal and lateral views. *Sol Energy* 2016;132:188–202.
- [21] Zhu Y, Shi J, Li Y, Wang L, Huang Q, Xu G. Design and experimental investigation of a stretched parabolic linear Fresnel reflector collecting system. *Energy Convers Manage* 2016;126:89–98.
- [22] Zhu Y, Shi J, Li Y, Wang L, Huang Q, Xu G. Design and thermal performances of a scalable linear Fresnel reflector solar system. *Energy Convers Manage* 2017;146:174–81.
- [23] Barbón A, Barbón N, Bayón L, Sanchez-Rodríguez JA. Parametric study of the small-scale linear Fresnel reflector. *Renew Energy* 2018;116:64–74.
- [24] Barbón A, Bayón L, Bayón-Cueli C, Barbón N. A study of the effect of the longitudinal movement on the performance of small scale linear Fresnel reflectors. *Renew Energy* 2019;138:128–38.
- [25] Barbón A, López-Smeets C, Bayón L, Pardellas A. Wind effects on heat loss from a receiver with longitudinal tilt angle of small-scale linear Fresnel reflectors for urban applications. *Renew Energy* 2020;162:2166–81.
- [26] Li D, Li Z, Zheng Y, Liu C, Hussein AK, Liu X. Thermal performance of a PCM-filled double-glazing unit with different thermophysical parameters of PCM. *Sol Energy* 2016;133:207–20.
- [27] Liu C, Wu Y, Li D, Ma T, Hussein AK, Zhou Y. Investigation of thermal and optical performance of a phase change material filled double-glazing unit. *J Build Phys* 2018;42:99–119.
- [28] Benabderrahmane A, Benazza A, Hussein AK. Heat transfer enhancement analysis of tube receiver for parabolic trough solar collector with central corrugated insert. *Trans ASME, J Heat Transfer* 2020;142:062001-1-062001-8.
- [29] Hussein AK. Applications of nanotechnology in renewable energies - A comprehensive overview and understanding. *Renew Sustain Energy Rev* 2015;42:460–76.
- [30] Hussein AK. Applications of nanotechnology to improve the performance of solar collectors - Recent advances and overview. *Renew Sustain Energy Rev* 2016;62:767–92.
- [31] Hussein AK, Walunj A, Kolsi L. Applications of nanotechnology to enhance the performance of the direct absorption solar collectors. *J Therm Eng* 2016;2:529–40.
- [32] Rostami S, Sepehrirad M, Dezfulizadeh A, Hussein AK, Goldanlou A, Shadloo M. Exergy optimization of a solar collector in flat plate shape equipped with elliptical pipes filled with turbulent nanofluid flow: A study for thermal management. *Water* 2020;12:2294–310.
- [33] Lee C, Chou P, Chiang C, Lin C. Sun tracking systems: A review. *Sensors* 2009;9:3875–90.
- [34] Mousazadeh H, Keyhani A, Javadi A, Mobli H, Abrinia K, Sharifi A. A review of principle and sun-tracking methods for maximizing solar systems output. *Renew Sustain Energy Rev* 2009;13:1800–18.
- [35] Bortolini M, Gamberi M, Graziani A, Manfroni M, Manzini R. Hybrid strategy for bi-axial solar tracking system. *J Control Eng Technol* 2012;2:130–44.
- [36] Mi Z, Chen J, Chen N, Bai Y, Fu R, Liu H. Open-loop solar tracking strategy for high concentrating photovoltaic systems using variable tracking frequency. *Energy Convers Manage* 2016;117:142–9.
- [37] Sidek MHM, Azis N, Hasan WZW, Ab Kadir MZA, Shafie S, Radzi MAM. Automated positioning dual-axis solar tracking system with precision elevation and azimuth angle control. *Energy* 2017;124:160–70.
- [38] Gregor R, Takase Y, Rodas J, Carreras L, Lopez A, Rivera M. A novel design and automation of a biaxial solar tracking system for PV power applications. *IEEE Industrial Electronics Society (IECON)*; 2013, p. 1484–9.
- [39] Roth P, Georgiev A, Boudinov H. Cheap two axis sun following device. *Energy Convers Manage* 2005;46:1179–92.
- [40] Rubio FR, Ortega MG, Gordillo F, Lopez-Martínez M. Application of new control strategy for sun tracking. *Energy Convers Manage* 2007;48:2174–84.
- [41] Barbón A, Bayón L, Barbón N, Otero JA, Bayón-Cueli C, Rodríguez L, et al. Concentrador solar lineal Fresnel con triple movimiento, Spain Patent ES 2601222 (B1), 2017.
- [42] Duffie JA, Beckman WA. *Solar engineering of thermal processes*. John Wiley & Sons; 2013.
- [43] Solidworks. *Technical reference*. Solidworks Corporation; 2018.
- [44] Barbón A, Sánchez-Rodríguez JA, Bayón L, Bayón-Cueli C. Cost estimation relationships of a small scale linear Fresnel reflector. *Renew Energy* 2019;134:1273–84.
- [45] Reda I, Andreas A. Solar position algorithm for solar radiation applications. *Sol Energy* 2004;76:577–89.
- [46] Michalsky JJ. The astronomical almanac's algorithm for approximate solar position (1950–2050). *Sol Energy* 1950;40:227–35.
- [47] Blanco-Muriel M, Alarcon-Padilla DC, Lopea-Moratalla T, Lara-Coira M. Computing the solar vector. *Sol Energy* 2001;70:431–41.
- [48] Grena R. An algorithm for the computation of the solar position. *Sol Energy* 2008;82:462–70.
- [49] Malav S, Vadhera S. Hardware implementation of solar tracking system using a stepper motor. In: IEEE international conference on energy, power and environment. 2015.
- [50] Jin X, Xu G, Zhou R, Luo X, Quan Y. A sun tracking system design for a large dish solar concentrator. *Int J Clean Coal Energy* 2013;2:16–20.
- [51] Abd Rahim R, Zainudin MNS, Ismail MM, Othman MA. Image-based solar tracker using raspberry pi. *J Multidiscip Eng Sci Technol* 2014;1(5):369–73.
- [52] Palomino LE, G. Alexandre. Solar radiation monitoring using electronic embedded system raspberry pi database connection MySQL, ubidots and TCS-230 sensor. In: IEEE Conf. CHILECON 2015.
- [53] Upton E, Halfacree G. *Raspberry pi user guide*. John Wiley & Sons; 2014.
- [54] DIGI. Technical data. 2020, Available from: <https://www.digi.com>. [Accessed on: 22 June 2020].
- [55] Texas Instruments. Technical data. 2020, Available from: <http://www.ti.com/lit/ds/symlink/uln2803a.pdf>. [Accessed on: 22 June 2020].
- [56] Arduino. Technical data. 2020, Available from: <http://www.arduino.cc/en/Main/ArduinoBoardMini>. [Accessed on: 22 June 2020].

- [57] U-blox. Technical data. 2020, Available from: [https://www.u-blox.com/sites/default/files/products/documents/NEO-6_DataSheet_\(GPS.G6-HW-09005\).pdf](https://www.u-blox.com/sites/default/files/products/documents/NEO-6_DataSheet_(GPS.G6-HW-09005).pdf). [Accessed on: 22 June 2020].
- [58] Maxim integrated. Technical data. 2020, Available from: <https://datasheets.maximintegrated.com/en/ds/MAX6675.pdf>. [Accessed on: 22 June 2020].
- [59] AVAGO. Technical data. 2020, Available from: <https://datasheet.octopart.com/ADNS-9800-Avago-datasheet-10666463.pdf>. [Accessed on: 22 June 2020].
- [60] Muneer T. Solar radiation and daylight models. Elsevier Butterworth - Heinemann; 2004.
- [61] Chong KK, Onubogu NO, Yew TK, Wong CW, Tan WC. Design and construction of active daylighting system using two-stage non-imaging solar concentrator. *Appl Energy* 2017;207:45–60.
- [62] VISHAY. Technical data. 2020, Available from: <https://www.vishay.com/docs/84286/veml7700.pdf>. [Accessed on: 22 June 2020].
- [63] PVGIS. Joint Research Centre (JRC), Available online: http://re.jrc.ec.europa.eu/pvg_tools/en/tools.html#PVP.
- [64] Barbón A, Fortuny Ayuso P, Bayón L, Fernández-Rubiera JA. Predicting beam and diffuse horizontal irradiance using Fourier expansions. *Renew Energy* 2020;154:46–57.
- [65] Barbón A, Bayón-Cueli C, Bayón L, Fortuny Ayuso P. Influence of solar tracking error on the performance of a small-scale linear Fresnel reflector. *Renew Energy* 2020;162:43–54.
- [66] Sharma VM, Nayak JK, Kedare SB. Effects of shading and blocking in linear Fresnel reflector field. *Sol Energy* 2015;113:114–38.
- [67] Theunissen PH, Beckman WA. Solar transmittance characteristics of evacuated tubular collectors with diffuse back reflectors. *Sol Energy* 1985;35:311–20.
- [68] Cagnoli M, Mazzei D, Procopio M, Russo V, Savoldi L, Zanino R. Analysis of the performance of linear Fresnel collectors: Encapsulated vs. evacuated tubes. *Sol Energy* 2018;164:119–38.
- [69] Binotti M, Manzolini G, Zhu G. An alternative methodology to treat solar radiation data for the optical efficiency estimate of different types of collectors. *Sol Energy* 2014;110:807–17.
- [70] Moghimi MA, Craig KJ, Meyer JP. A novel computational approach to combine the optical and thermal modelling of linear Fresnel collectors using the finite volume method. *Sol Energy* 2015;116:407–27.
- [71] Bruck M, Sandborn P, Goudarzi N. A levelized cost of energy (LCOE) model for wind farms that include power purchase agreements (PPAs). *Renew Energy* 2018;122:131–9.
- [72] Tran TTD, Smith AD. Incorporating performance-based global sensitivity and uncertainty analysis into LCOE calculations for emerging renewable energy technologies. *Appl Energy* 2018;216:157–71.
- [73] Bayón-Cueli C, Barbón A, Bayón L, Barbón N. A cost-energy based methodology for small-scale linear Fresnel reflectors on flat roofs of urban buildings. *Renew Energy* 2020;146:944–59.
- [74] IRENA. Renewable energy technologies: Cost analysis series (CSP). International Renewable Energy Agency; 2012.